The Astronomical Journal, 155:197 (9pp), 2018 May https://doi.org/10.3847/1538-3881/aab8ff

OSSOS. VIII. The Transition between Two Size Distribution Slopes in the Scattering Disk

S. M. Lawler[1], C. Shankman[1,2,3], J. J. Kavelaars[1,2], M. Alexandersen[4], M. T. Bannister[5], Ying-Tung Chen (陳英同)[4], B. Gladman[6], W. C. Fraser[5], S. Gwyn[1], N. Kaib[7], J.-M. Petit[8], and K. Volk[9]
[1] NRC-Herzberg Astronomy and Astrophysics, National Research Council of Canada, Victoria, BC, Canada
[2] Department of Physics and Astronomy, University of Victoria, Victoria, BC, Canada
[3] City of Toronto, Toronto, ON, Canada
[4] Institute of Astronomy and Astrophysics, Academia Sinica, Taipei, Taiwan
[5] Astrophysics Research Centre, Queen's University Belfast, Belfast, UK
[6] Department of Physics and Astronomy, The University of British Columbia, Vancouver, BC, Canada
[7] HL Dodge Department of Physics & Astronomy, University of Oklahoma, Norman, OK, USA
[8] Institut UTINAM, CNRS-Université de Franche-Comté, Besançon, France
[9] Lunar and Planetary Laboratory, University of Arizona, Tucson, AZ, USA
Received 2017 December 15; revised 2018 March 16; accepted 2018 March 20; published 2018 April 19

Abstract

The scattering trans-Neptunian Objects (TNOs) can be measured to smaller sizes than any other distant small-body population. We use the largest sample yet obtained, 68 discoveries, primarily by the Outer Solar System Origins Survey (OSSOS), to constrain the slope of its luminosity distribution, with sensitivity to much fainter absolute H-magnitudes than previous work. Using the analysis technique in Shankman et al., we confirm that a single slope for the H-distribution is not an accurate representation of the scattering TNOs and Centaurs, and that a break in the distribution is required, in support of previous conclusions. A bright-end slope of $\alpha_b = 0.9$ transitioning to a faint-end slope α_f of 0.4–0.5 with a differential number contrast c from 1 (a knee) to 10 (a divot) provides an acceptable match to our data. We find that break magnitudes H_b of 7.7 and 8.3, values both previously suggested for dynamically hot Kuiper Belt populations, are equally non-rejectable for a range of α_f and c in our statistical analysis. Our preferred divot H-distribution transitions to $\alpha_f = 0.5$ with a divot of contrast $c = 3$ at $H_b = 8.3$, while our preferred knee H-distribution transitions to $\alpha_f = 0.4$ at $H_b = 7.7$. The intrinsic population of scattering TNOs required to match the OSSOS detections is 3×10^6 for $H_r < 12$, and 9×10^4 for $H_r < 8.66$ ($D \gtrsim 100$ km), with Centaurs having an intrinsic population two orders of magnitude smaller.

Key words: Kuiper belt: general

1. Introduction

The populations of small bodies in our solar system are incrementally grinding themselves into dust through mutual collisions. On short timescales, collisions are infrequent, though on occasion, the aftermath can be directly observed (e.g., Jewitt et al. 2010). Over the age of the solar system, collisions may be the main force that shaped the observed size distribution of all but the largest trans-Neptunian objects (TNOs; Schlichting et al. 2013), or the size distribution may be a result of formation conditions (Fraser et al. 2014). As dynamical evolution is not size-dependant for these small TNOs, we do not expect the size distribution to be affected by removal of TNOs from the scattering population due to interactions with the giant planets. The size distribution of populations that are shaped by collisions can be described by a power law of the form $\frac{dN}{dD} \propto D^{-q}$, where an idealized infinite collisional cascade will produce an exponent of $q = 3.5$ (Dohnanyi 1969).

In the outer solar system, the luminosity distribution must be used as a proxy for the size distribution, because TNOs are unresolved. Luminosity is measured as an apparent magnitude, which can be directly converted to an absolute magnitude H when combined with a measured distance. The H-magnitude can then be directly mapped to diameter, as long as an albedo is measured (or assumed). A handful of small ($H \sim 9$–14) TNOs and Centaurs have had their albedos measured observationally, and they range from 4% to 16% (Duffard et al. 2014). The size distribution can be written in terms of absolute magnitude H as $\frac{dN}{dH} \propto 10^{\alpha H}$, where the size distribution exponent q is related to the H-magnitude exponent α by $q = 5\alpha + 1$ (assuming albedo is size-independent; Irwin et al. 1995; Fraser et al. 2008; Petit et al. 2008).

Measuring the size distribution of a small-body population tells us about their composition, collisional processes that shape them, and may also provide information on their formation. Collisional simulations of the asteroid belt (e.g., Bottke et al. 2005; Pan & Schlichting 2012) have found that the sizes of the largest asteroids are set by the initial formation sizes, which in combination with mass depletion of the asteroid belt (caused by Jupiter's migration), sets any structure in the size distribution. The size distribution of the asteroids can be measured to much smaller sizes (larger H-magnitudes) than the TNOs due to the fact that it is much closer, and thus smaller objects will be above survey detection limits. The asteroid size distribution at smaller sizes shows intriguing structure, which collisional simulations have shown to likely be caused by a combination of formation size and the initial number density of the asteroid belt; the transition between primordial and collisionally evolved populations happens at ~10–100 km (Bottke et al. 2005; Morbidelli et al. 2009a). By measuring the size distribution of the Kuiper Belt across several orders of magnitude in size, as has been done in the asteroid belt, we may gain an additional constraint on the timing and manner of Neptune's migration, which severely depleted the mass of the Kuiper Belt (Malhotra 1995; Gomes et al. 2004; Nesvorný 2015).

The magnitude distribution of the Kuiper Belt has long been modeled as a single slope at large sizes (e.g., Jewitt et al. 1996).

Gladman et al. (2001) found that the smallest TNOs had a size distribution inconsistent with a single power law. Later, Bernstein et al. (2004) measured a rollover, proving that a single power law was not adequate to describe the observed Kuiper Belt. Surveys are now reaching deep enough and detecting enough TNOs that additional structure in the size distribution is required to match observations (Fuentes & Holman 2008; Shankman et al. 2013, 2016; Fraser et al. 2014; Alexandersen et al. 2016).

Here, we focus our analysis on the scattering TNOs and Centaurs. Because they come closer to the Sun than most TNOs, we can observe smaller TNOs within this population than any other in the Kuiper Belt. Scattering TNOs and Centaurs are part of the dynamically "hot" population. TNOs in the dynamically hot population have had their orbits excited to higher inclinations and eccentricities by scattering off Neptune or past/current entanglement with mean-motion resonances (Gladman 2005). Previous work has demonstrated that the hot population, due to its different collisional and formation history, has a different size distribution than the dynamically cold population of the main classical Kuiper Belt (Petit et al. 2011; Fraser et al. 2014). We specifically exclude those TNOs that are currently resonant from the analysis presented in this manuscript, as they are likely to have experienced a different pathway to dynamical excitation than the scattering TNOs and Centaurs (i.e., Gladman et al. 2012).

Shankman et al. (2016) used scattering TNOs detected in four well-characterized surveys to measure the scattering TNO H-distribution to great precision. In this work, we provide an update for the measurement of the scattering TNO H-distribution with the inclusion of the full discovery data set of the Outer Solar System Origins Survey (OSSOS; Bannister et al. 2016; the full data set is in Bannister et al. 2018). OSSOS has completed its observing, more than tripling the sample of scattering TNOs and Centaurs since the analysis of Shankman et al. (2016).

The analysis here builds on the work of Shankman et al. (2016), using the same methodologies. We first discuss the OSSOS survey, summarizing the mechanics of the Survey Simulator, which allows us to forward-bias our model to allow statistical comparison with our observational sample of TNOs. In Section 3, we summarize the statistical analysis that we use to find the range of acceptable H-magnitude distributions allowed by our observed sample. Section 4 includes our population measurements, and in Section 5, we discuss how our measurements of the scattering disk fit into the larger context of the solar system.

2. Scattering Sample Selection

Because scattering TNOs and Centaurs have high eccentricities, and their pericenter distances can range from nearly Jupiter-crossing to >40 au, the observing biases are extreme and must be accounted for carefully; e.g., small Centaurs and TNOs with closer pericenters are far more likely to be detected in magnitude-limited surveys (as is visible in Figure 1). By using only TNOs detected by well-characterized surveys in this analysis, where the magnitude limits, pointings, and tracking efficiencies are known and published,[10] we are able to forward-bias models of the scattering disk and statistically compare the resulting biased simulated detections with the real TNO discoveries.

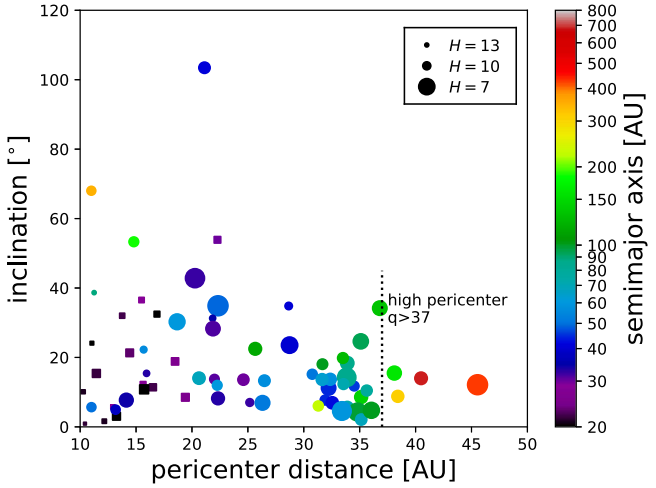

Figure 1. Orbital properties (pericenter distance q and inclination i) of the 68 TNOs detected by the OSSOS ensemble of surveys (see Table 3 in the Appendix, and Table 3 in Bannister et al. 2018) that are classified as scattering (circles) or Centaurs (squares; see Section 2 for details on classification). Semimajor axis a is shown via point color, most of these TNOs have $a < 200$ au. Point sizes are proportional to diameter (assuming the same albedo); note that the closest objects are preferentially small due to discovery biases. Outside $q > 37$ au (noted with dotted line in plot), scattering TNOs have preferentially larger a and are more weakly bound. See the text for further discussion.

OSSOS is a large program on the Canada–France–Hawaii Telescope over five years to discover TNOs while carefully characterizing tracking fractions, detection efficiencies, and pointing directions, allowing the survey biases to be fully quantified (Bannister et al. 2016). This methodology has been followed for three other large Kuiper Belt surveys: The Canada–France Ecliptic Plane Survey (CFEPS; Petit et al. 2011), the CFEPS high latitude component (HiLat; Petit et al. 2017), and the survey of (Alexandersen et al. 2016, hereafter referred to as MA). Combining these three surveys with OSSOS gives a well-characterized set of surveys (which we refer to throughout this paper as the "OSSOS ensemble"), whose combined detected TNOs provide powerful constraints on the intrinsic TNO orbital distributions and populations when used in combination with the Survey Simulator. This statistical reproduction of the survey biases is discussed extensively in other works, (e.g., Kavelaars et al. 2009; Petit et al. 2011; Bannister et al. 2016; Shankman et al. 2016; Lawler et al. 2018).

Shankman et al. (2016) analyzed a scattering TNO sample of 22 objects from CFEPS, HiLat, MA, and the first two (of eight) observing blocks of OSSOS. OSSOS has since detected dozens of new scattering TNOs and Centaurs, bringing the full sample available for analysis to 68 TNOs (17 Centaurs, 51 scattering). The orbital elements of the full sample analyzed here are shown in Figure 1 and Table 3 in the Appendix, and further detail is available in Table 3 (ensemble catalog) in Bannister et al. (2018).

Here, we use the dynamical classification scheme of Gladman et al. (2008) to determine membership in the scattering and Centaur classes. These two classes are both unstable on timescales much shorter than the age of the solar system. The distinction between them is semimajor axis a relative to Neptune's orbit; Centaurs have smaller a and

[10] Survey Simulator code and OSSOS ensemble survey pointings are publicly available at https://github.com/OSSOS/SurveySimulator, and properties of TNOs detected by the OSSOS ensemble are published in Bannister et al. (2018).

scattering TNOs have larger (shown by different symbols in Figure 1). Their changes in a over time are usually due to close encounters with one of the giant planets, but can also be due to dynamical diffusion for the more weakly bound TNOs (Bannister et al. 2017): those that have largest pericenter distances $q > 37$ au tend to also have the largest semimajor axes of the sample (see Figure 1). The Centaurs show similar evolution in semimajor axis and represent the low-a tail of the scattering population (e.g., Gomes et al. 2008), thus it is expected that they will share the same H-distribution.

3. Measuring the True H-distribution

Previous work has shown that there is a sharp transition in the H-distribution of the TNOs, though the form of the transition is unclear (Shankman et al. 2013, 2016; Fraser et al. 2014; Alexandersen et al. 2016). We parameterize this transition using a bright-end slope α_b, a faint-end slope α_f, a break magnitude H_b, and a differential contrast c. We use the terminology that $c = 1$ is a knee, $c > 1$ is a divot. We refer the reader to Figure 9 in Shankman et al. (2016) for a graphical demonstration of the effect of these two different transitions on the cumulative and differential number distributions in H.

The slope at the bright end of the TNO H-distribution α_b, a range of $H \simeq 4$–7, is well-probed by previous work (e.g., Fraser & Kavelaars 2009; Petit et al. 2011). Our OSSOS ensemble detections range from H_r values of 6 to 14.5 because of the very close pericenter distances of some of these TNOs, and thus this analysis is sensitive to a much fainter H_r range than previous work. We note that several of the scattering TNOs included in this sample were not observed in r-band because some blocks of CFEPS observed only in g. These have had their g-band and H_g magnitudes transposed to r by assuming that $g - r = 0.7$, which is at the neutral end of the observed color range of dynamically excited TNOs (Tegler et al. 2016). Shankman et al. (2016) used $g - r = 0.7$, and also demonstrated that using $g - r$ values ranging from 0.5 to 0.9 makes no difference to the statistical analysis performed below (see Figure 8 in Shankman et al. 2016).

In this analysis, as in previous work (Shankman et al. 2013, 2016), we seek to measure the slope of the faint end of the H-distribution α_f, the contrast of the transition c, and the H-magnitude where the break occurs H_b. We test H-distributions from a grid covering α_f from 0.1 to 0.9, and c from 1 to 100, with two different break magnitudes, $H_b = 8.3$ (preferred break magnitude from Shankman et al. 2016) and $H_b = 7.7$ (preferred break magnitude from Fraser et al. 2014).

3.1. The Survey Simulator and Statistical Analysis

Our method of forward-biasing a model distribution with different H-distributions is discussed in detail in Shankman et al. (2013) and Shankman et al. (2016). Briefly, we start with a version of the scattering distribution modeled by the emplacement simulation of Kaib et al. (2011), with the dynamically hotter inclination distribution used in Shankman et al. (2016). We then draw orbits from this simulation. Orbits are randomly oriented (random ω and Ω), and objects are placed with a random mean anomaly on these orbits (which sets the distance), and are given an H-magnitude from within a chosen H-distribution, and then an r-magnitude is calculated. The Survey Simulator then determines if that r-magnitude, rate of motion, and on-sky position was detectable in the OSSOS survey ensemble. This process is continued until a large number (hundreds) of simulated detections are created. The cumulative distributions of simulated detections are then statistically compared with the cumulative distributions of the 68 real Centaurs and scattering TNOs in semimajor axis a, inclination i, r-magnitude m_r, pericenter distance q, distance at detection d, and H-magnitude in r-band H_r. These six cumulative distributions are shown in Figure 2 for the real TNOs as well as simulated detections using three different H-distributions.

The statistical analysis is described in detail in Shankman et al. (2016), and we summarize below. We first calculate the Anderson–Darling (AD) statistic (Anderson & Darling 1954), comparing the observed TNOs and the simulated detections for a given H-distribution. An AD statistic is computed for each parameter. From previous work, we found that the most powerful lever arms for this analysis (because they vary most for different modeled H-distributions) come from using the parameters q, d, and H_r, so we sum the AD statistics calculated for each of these three distributions (following the analysis method of Parker 2015). This summed AD statistic is bootstrapped by selecting at random 68 objects from the distribution of simulated detections, calculating the AD statistic between this random sample and the simulated detections in each parameter, and summing them. This random selection and AD statistic calculation is repeated hundreds of times. The distribution of summed AD statistics for random samples of the simulated distribution is then compared to the summed AD statistic for the real TNOs. If that AD statistic or larger occurs for $<5\%$ of the random distributions, we can reject that distribution with $>2\sigma$ ($>95\%$) confidence. To explain in another way, if $<95\%$ of random subsets of the model are farther from the parent model than the observations are, then the model cannot be rejected.

3.1.1. The Scattering Inclination Distribution

Figure 2 shows a good match between the observations and the preferred model for five of the six parameters measured; the inclination distribution has a rather poor fit at high inclinations (this is true for all H-distributions tested). The paucity of high-inclination objects in the model as compared with observations was noted and discussed in Shankman et al. (2016). The difficulty of generating high-inclination objects in emplacement models is a well-noted problem (e.g., Kaib et al. 2011), and suggests that a small fraction of scattering TNOs may require a different emplacement pathway in order to match the real Kuiper Belt. Suggested mechanisms in the literature include diffusion from the Oort Cloud (Kaib et al. 2009; Brasser et al. 2012), interaction with a distant massive planet (Gomes et al. 2015), and interaction with a rouge planet that was later ejected from the solar system (Gladman & Chan 2006). Creating dynamical emplacement models of the Kuiper Belt that obtain a realistic inclination distribution is currently an area of active research.

We perform a simple experiment to make sure that the inclination distribution does not severely affect the three parameters we test (H, d, and q) by doubling and halving all of the inclinations in the model and re-running our statistical test. We find that the bootstrapped AD values only vary by 1%–2% for these two very different inclination distributions, and so we conclude that while the inclination distribution shown in Figure 2 does not provide a great match to observations, the other properties of the model still provide an excellent fit to the real scattering TNOs.

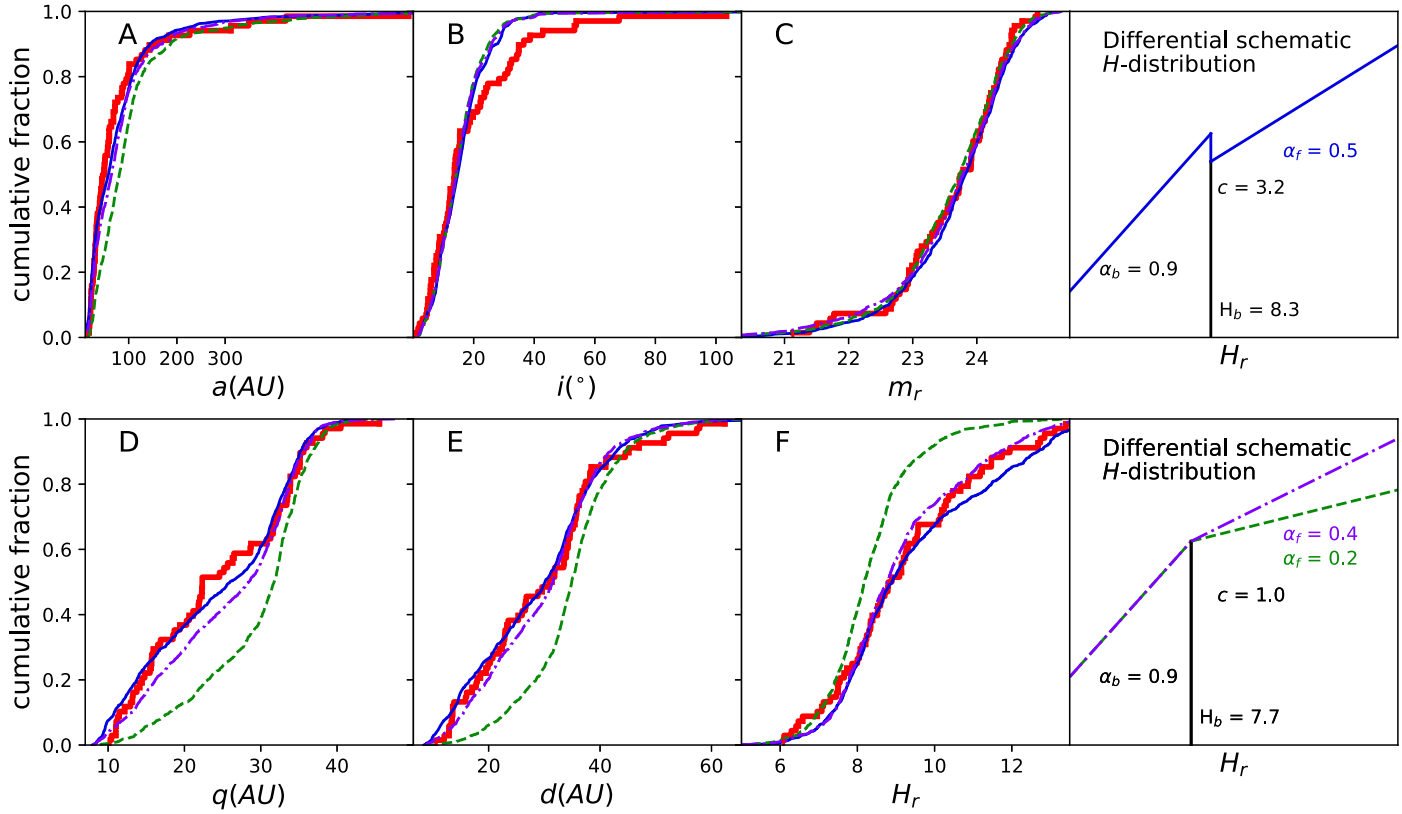

Figure 2. Cumulative distributions across six parameters for the 68 observed scattering TNOs and Centaurs (red step-function), and three candidate *H*-distributions. Panels (A–F) correspond to the semimajor axis a, inclination i (see Section 3.1.1), magnitude at detection in r-band m_r, pericenter q, distance at detection d, and H-magnitude in r-band, respectively. The rightmost panel provides schematics for three different H-distributions: (1) our preferred (c, α_f) pair (solid blue line) (2) our preferred knee distribution (dotted–dashed purple line) and (3) the best-fit knee distribution from Fraser et al. (2014) (dashed green line).

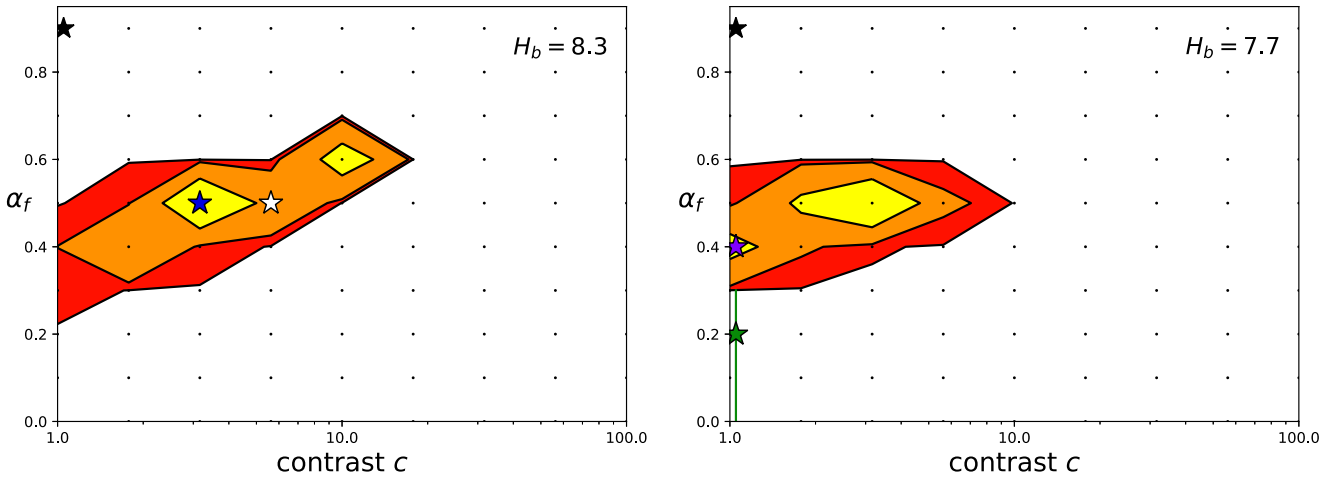

Figure 3. Contours of the rejectability for the tested faint-end slope α_f and contrast c pairs with a break located at $H_b = 8.3$ (left) and $H_b = 7.7$ (right); all models tested use $\alpha_b = 0.9$. The contours represent the 1σ, 2σ and 3σ rejectability levels with white being rejectable at $>3\sigma$, red being rejectable at $>2\sigma$, and orange and yellow not statistically rejectable. Stars highlight notable (α_f, c) pairs: the dark blue, green, and purple stars show models that are also plotted in the same color in Figure 2. The dark blue star denotes our preferred (α_f, c) pair (see Section 3.2), the green star (with 1σ error bars) denotes the best-fit knee model for dynamically hot TNOs from Fraser et al. (2014), and the purple star is our preferred knee model. For comparison with previous work, the white star denotes the preferred (α_f, c) pair from Shankman et al. (2016), and the black star denotes a single slope of $\alpha = 0.9$ (identical in both plots), and is strongly rejectable.

3.2. Preferred H-distribution

Using the 68 detected scattering TNOs and Centaurs from the OSSOS ensemble, we find that the least-rejectable *H*-distribution is for $\alpha_f = 0.5$ and $c = 3.2$, using $\alpha_b = 0.9$. This *H*-distribution is shown as a blue solid line in Figure 2, and by a blue star in Figure 3.

We are unable to statistically reject a knee distribution. A transition to a faint slope $\alpha_f = 0.4$ at $H_b = 7.7$ is non-rejectable at 3σ significance in our analysis; this preferred knee *H*-distribution is shown by a purple dashed–dotted line in Figure 2 and by a purple star in Figure 3. For comparison, the best-fit knee distribution from Fraser et al. (2014) is shown with a green star, including 1σ error bars.

Table 1
Population Estimates for Scattering TNOs

H_b	α_f	c	$H_r < 8.66$ Population	$H_r < 10$ Population	$H_r < 12$ Population	Comment
8.3	0.5	3.2	$(0.9 \pm 0.2) \times 10^5$	$(2.9 \pm 0.7) \times 10^5$	$(2.7 \pm 0.7) \times 10^6$	preferred divot, this work
7.7	0.4	1	$(0.8 \pm 0.2) \times 10^5$	$(3.5^{+0.9}_{-0.6}) \times 10^5$	$(2.4^{+0.6}_{-0.4}) \times 10^6$	preferred knee, this work
8.3	0.5	5.6	$(1.0^{+0.3}_{-0.2}) \times 10^5$	$(2.6^{+0.7}_{-0.5}) \times 10^5$	$(2.1^{+0.6}_{-0.4}) \times 10^6$	preferred, Shankman et al. (2016)
8.3	0.4	1	$(0.8 \pm 0.2) \times 10^5$	$(4.0 \pm 0.9) \times 10^5$	$(2.8^{+0.6}_{-0.7}) \times 10^6$	least-rejectable knee, $H_b = 8.3$
7.7	0.5	3.2	$(0.7 \pm 0.2) \times 10^5$	$(2.8^{+0.7}_{-0.6}) \times 10^5$	$(2.7^{+0.7}_{-0.6}) \times 10^6$	least-rejectable divot, $H_b = 7.7$
			Previously Published Population Estimates			
8.3	0.5	5.6			$\sim 1 \times 10^6$	estimate from Shankman et al. (2013)
8.3	0.5	5.6			$(2.4–8.3) \times 10^5$	estimate from Shankman et al. (2016)
–	0.8	–	$(5^{+5}_{-3}) \times 10^3$		$(4^{+4}_{-3}) \times 10^6$	CFEPS estimate (Petit et al. 2011)

Note. Error bars on population estimates are 95% confidence intervals.

The preferred divot H-distribution from Shankman et al. (2016) remains a viable explanation for the scattering TNO H-distribution (white star in Figure 3), but the analysis here increases the number of rejectable models, more tightly constraining the acceptable parameter space of α_f and c. As in Shankman et al. (2013, 2016), a single power law ($c = 1$, $\alpha_f = \alpha_b = 0.9$) is rejectable at $>3\sigma$ significance (shown with a black star in both plots in Figure 3).

Interestingly, we are not able to rule out either break magnitude H_b we tested. We tested two different values of H_b: 8.3 and 7.7, based on predictions from previous work (Fraser et al. 2014; Shankman et al. 2016). The yellow contours in Figure 3 highlight the H-distributions, which are rejectable by our analysis at the lowest significance (i.e., least-rejectable distributions). Contours of $<1\sigma$ rejectability occur for both H_b values that we tested, and ($\alpha_f = 0.5$, $c = 3.2$) are the least-rejectable H-distributions for both values of H_b.

4. The Intrinsic Population Size

We use the Survey Simulator to determine the number of scattering TNOs and Centaurs brighter than a given H-magnitude that must be drawn from the Kaib et al. (2011) scattering TNO model to allow 68 detections (Table 1: scattering TNOs), or 17 detections from the $a < 30$ au subset of the Kaib et al. (2011) scattering TNO model (Table 2: Centaurs). Error bars on these intrinsic populations are calculated by running this experiment many times and finding the populations that bracket 95% of the estimates; the error bars given are thus 95% confidence intervals on the intrinsic population.

4.1. The Size of the Scattering TNO Population

Using our preferred H-distribution ($H_b = 8.3$, $\alpha_f = 0.5$, $c = 3.2$), the population must be $(2.7^{+0.6}_{-0.5}) \times 10^6$ for $H_r < 12$ (which corresponds to $D \gtrsim 20$ km for an albedo of 0.04), and $(8 \pm 2) \times 10^4$ for $H_r < 8.66$ (which corresponds to $D \gtrsim 100$ km for an albedo of 0.04). Interestingly, using other statistically acceptable H-distributions does not cause the population to vary by more than a very small factor; the population estimates from all statistically acceptable H-distributions are consistent within the 95% error bars.

Table 1 lists population estimates using several different H-distributions that are statistically acceptable in our analysis, as well as comparisons with previously published scattering population estimates. Our population estimates here are slightly higher than those reported in Shankman et al. (2013) and Shankman et al. (2016). CFEPS (Petit et al. 2011) estimates a population of 5000^{+5000}_{-3000} scattering TNOs for $H_g < 9.16$ ($H_r \lesssim 8.66$), much smaller than our population estimate. However, after scaling by the assumed single slope of $\alpha = 0.8$ down to $H_r < 12$ gives $(4^{+4}_{-3}) \times 10^6$, consistent with our population estimates, albeit with very large error bars.

Assuming that this size distribution holds for another order of magnitude smaller in TNO size, we can scale our population estimates up to include TNOs at very small sizes ($H < 18$), and compare with the number of scattering TNOs that are required to supply the observed population of Jupiter Family Comets (JFCs). However, this close-in population has been measured to have slightly shallower slopes (Snodgrass et al. 2011; Fernández et al. 2013; Bauer et al. 2017) than the faint slope α_f found in this analysis, so this may not be a valid assumption. With our preferred H-distribution, we find that the scattering population down to $H < 18$ should include 3×10^9 objects, which is a large enough supply to be the origin of the Jupiter Family Comets (Volk & Malhotra 2008).

4.2. The Size of the Centaur Population

The intrinsic Centaur population is about two orders of magnitude smaller than the intrinsic scattering TNO population, consistent with their shorter dynamical lifetime. In Table 2, we compare our Centaur population estimates with the population estimates of temporary Uranian and Neptunian co-orbitals in Alexandersen et al. (2016) and the abundance of these relative to $a < 34$ au scattering objects estimated in Alexandersen et al. (2013). Alexandersen et al. (2013) gives the fraction of the $a < 34$ au scattering population that must be trapped as temporary co-orbitals with Neptune and Uranus at any given time. The orbital distributions from Parker (2015) and Alexandersen et al. (2013) are combined with a knee H-distribution similar to the best fit of Fraser et al. (2014) and a divot distribution similar to the preferred H-distribution from Shankman et al. (2016) to calculate the population estimates in Table 2. The Centaur population estimates from our analysis are much smaller, but are not inconsistent when taking into account the (very large) error bars and upper limits from Alexandersen et al. (2013, 2016).

Table 2
Population Estimates for Centaurs

H_b	α_f	c	$H_r < 8.66$ Population	$H_r < 10$ Population	$H_r < 12$ Population	Comment
8.3	0.5	3.2	110^{+60}_{-40}	390^{+200}_{-150}	3500^{+1800}_{-1400}	preferred divot, this work
7.7	0.4	1	130^{+80}_{-70}	550^{+340}_{-290}	3700^{+2300}_{-2000}	preferred knee, this work
			Previously Published Population Estimates			
7.7	0.2	1	⩽75,000	$(2.8^{+10.0}_{-2.5}) \times 10^4$		calculated from Uranian co-orbitals[a]
8.5	0.5	6	⩽75,000	$(2.8^{+13.0}_{-2.5}) \times 10^4$		calculated from Uranian co-orbitals[a]
7.7	0.2	1	$2500^{+11,000}_{-2100}$	$7100^{+32,000}_{-6800}$		calculated from Neptunian co-orbitals[a]
8.5	0.5	6	$2900^{+11,000}_{-2500}$	$7500^{+32,000}_{-7100}$		calculated from Neptunian co-orbitals[a]

Note. Error bars on population estimates are 95% confidence intervals.
[a] Calculated from observations and models of Alexandersen et al. (2013, 2016). Note that populations here are actually for the $a < 34$ au scattering population, a large fraction of which will be Centaurs; see the text.

Another way we can make use of the Survey Simulator is to estimate how many relatively large Centaurs should exist based on our preferred H-distribution. Using this methodology, we find that the expected number of $H_r < 6$ Centaurs is ⩽1 with 95% confidence. Reassuringly, the largest known Centaur, (10199) Chariklo, has an H_r magnitude of 6.82 ± 0.02 (assuming a linear spectrum and no phase correction; Peixinho et al. 2015).

5. Discussion

Although we are unable to formally reject either a knee or divot distribution, the power of forward-biasing combined with statistical analysis of the full OSSOS data set has vastly reduced the allowed parameter space compared to previous analyses (Shankman et al. 2013, 2016). But even with the earlier much smaller number of detections, this analysis technique is powerful. While the range of parameter space that was non-rejectable in Shankman et al. (2013) was many times larger than in our analysis here, the preferred divot from the analysis in Shankman et al. (2013) still provides a good agreement to the fit obtained here, even though that analysis only included 11 TNOs, while the analysis here contains over six times as many TNOs.

5.1. Knee or Divot?

This analysis has shown that a divot fits the data slightly better than a knee distribution, but knees cannot be rejected for several values of α_f. For the break at larger TNO sizes, $H_b = 7.7$, α_f of 0.4–0.5 and c from 1 (knee) to 5.6 are non-rejectable. For the $H_b = 8.3$ break, a slightly larger parameter space is non-rejectable, encompassing α_f from 0.3 to 0.6, and c from 1 to 10.

Our preferred knee distribution has a slightly steeper slope ($\alpha_f = 0.4$) than the best-fit knee H-distribution found by the analysis of Fraser et al. (2014) ($\alpha_f = 0.2$). However, the 1σ uncertainties the published uncertainties on the Fraser et al. (2014) faint-end slope fit allow up to $\alpha_f = 0.3$, which is just inside the contour of non-rejectability (Figure 3, right panel), and is thus non-rejectable by our analysis.

5.2. Comparison with Other TNO Populations

This analysis is in broad agreement with the luminosity functions found for other dynamically hot populations in the Kuiper Belt.

Fraser et al. (2014) reports a α_f slope of 0.36, with a break magnitude $H_b = 8.4$ for the Trojan asteroids, which is acceptable in our analysis and would thus allow a common H-distribution for the two populations. If the Kuiper Belt was emplaced by scattering off the giant planets during a period of instability (Morbidelli et al. 2005; Nesvorný et al. 2013), the Trojans would also be drawn from this population and should have the same size distribution (Morbidelli et al. 2009b). Determining whether or not the Trojans and dynamically hot Kuiper Belt populations share a size distribution is an important test of this model and is an area of active research (e.g., Wong & Brown 2015; Yoshida & Terai 2017).

While the number of detected Neptune Trojans is small, previous surveys have noted that there appears to be a lack of small members (Sheppard & Trujillo 2010; Parker 2015), which would be consistent with a divot in the size distribution.

The plutinos (TNOs in the 3:2 mean-motion resonance with Neptune) constitute the closest well-populated resonance, so studies are able to probe the size distribution down to smaller sizes than any other resonance. The well-characterized survey of Alexandersen et al. (2016) performs a similar analysis to this work and found that a break is required in the plutino size distribution, with a range of contrasts (including 1), break magnitudes, and faint-end slopes that match their H-distribution of plutino detections. Their preferred divot H-distribution is similar to the preferred divot of this work with a steeper faint-end slope: $c = 6$ and $\alpha_f = 0.8$ at $H_b = 8.4$ (though their non-rejectable parameter space covers a large range of α_f and c values, see Figure 10 in Alexandersen et al. 2016). Knee distributions also provide a statistically acceptable match to their plutino detections, with their preferred fit exactly matching ours ($\alpha_f = 0.4$ at $H_b = 7.7$) and consistent with the best fit in Fraser et al. (2014).

Volk et al. (2016), which used detections only from the first two (of eight) OSSOS observing blocks, find no evidence in favor of a break in the size distribution, but show that this could be an effect of small number statistics. The analysis of the plutinos in the full OSSOS survey has several times more detected plutinos, and a transition is required in the H-distribution to match these

observations; however, both a knee or divot transition provide reasonable matches to the data (Volk et al. 2017).

We note that previous analysis of the dynamically hot classical TNOs prefers a bright-end slope $\alpha_b = 0.8$ (95% confidence range 0.6–1.1, see Figure 5 in Petit et al. 2011), and ongoing analysis on the OSSOS discoveries indicates perhaps an even shallower slope provides a better fit to the larger TNOs (J.-M. Petit et al. 2018, in preparation). Our bright-end slope of $\alpha_b = 0.9$ is consistent with our data and with previous analysis of dynamically hot populations (e.g., Gladman et al. 2012), but as more relatively bright TNOs are discovered by current and future all-sky surveys (e.g., Holman et al. 2018), the best fit for the bright-end slope should be revisited.

5.3. Comparison with the Cratering Record

The distribution of craters on a planetary surface can be used to infer the distribution of impactor sizes if one understands the orbital distribution (and thus planetary impact speed distribution) of the projectiles. Due to its orbital inclination and Kozai oscillation while inside the 3:2 mean-motion, Pluto spends a large fraction of its time at latitudes above the dynamically cold classical belt, and its orbital eccentricity results in it spending little time passing through the cold classical Kuiper Belt (Greenstreet et al. 2015); the majority of its impacting projectiles thus come from dynamically hot populations, and it is therefore the dynamically hot population's size distribution that will be encoded in the crater counts.

Using imaging from the *New Horizons* spacecraft's Pluto encounter (Stern et al. 2015; Moore et al. 2016) and crater-rate production calculations (Greenstreet et al. 2015), the distribution of impactor sizes has been estimated to arise from an H-distribution with $\alpha \simeq 0.4$ for projectiles with $H = 13$–19 (projectile diameters of 1–20 km; Singer et al. 2016). This H range just barely overlaps with our present analysis, which covers $H \simeq 6$–13, but this joint data set implies a roughly constant index α could extend from the break near $D \sim 100$ km down to $H \simeq 19$ ($D \simeq 1$ km). If the faint-end slope we measure does indeed continue to $D \simeq 1$ km, this is additional support for the scattering disk being the sole source of the JFCs, as this assumption was made above (Section 4) to calculate the population size that was in agreement with this requirement. For even smaller objects, recent results of the Charon crater-field analysis indicate that the Kuiper Belt's α becomes even shallower (Singer et al. 2018), but sub-km TNOs are beyond the reach of ground-based and even space-based near-Earth telescopes.

6. Summary and Conclusions

This work is an exploration of the scattering TNO H-distribution with the full OSSOS sample, expanding on the analysis of Shankman et al. (2016) with a threefold larger set of detections (68 rather than 22 TNOs) and including fainter H_r magnitudes than previous work. We have demonstrated that existing models (H-distributions with either a divot or knee transition from bright- to faint-end slopes) provide acceptable matches for the H-distribution observed for scattering TNOs, but we have greatly constrained the allowed parameter space of possible faint slopes α_f and contrasts of the transition. Our preferred H-distribution has a bright-end slope $\alpha_b = 0.9$, a faint slope $\alpha_f = 0.5$, and a divot of contrast $c = 3.2$, though a knee distribution with $\alpha_f = 0.4$ is also acceptable. The H-magnitude at the break is not important to our fit, and we find equally statistically acceptable H-distributions for $H_b = 7.7$ or 8.3, both of which were proposed by previous analyses. Large surveys such as Pan-STARRS and LSST will detect many new TNOs, especially at relatively bright H-magnitudes, and that will likely provide more statistical constraint on exactly where the break magnitude is, providing more information on the initial planetesimal formation size and collisional history of the Kuiper Belt.

We find that the shallower slope at faint magnitudes makes populations that are consistent with both the cratering record on Pluto and the population required to be the source of the Jupiter Family Comets.

A full exploration of possible size distributions would be best done in the context of a formation and evolutionary model of the solar system. The current degeneracy across potential break locations and divot or knee distributions may be addressed through additional constraints from formation theories. In order to explore this, one must understand the conditions under which accretion takes place, e.g., born big (Morbidelli et al. 2009a) or pebble accretion (Shannon et al. 2016), and must also understand the dynamical excitation process, e.g., whether Neptune's migration was smooth (Hahn & Malhotra 2005), grainy (Nesvorný & Vokrouhlický 2016), or chaotic (Tsiganis et al. 2005). By using these dynamical constraints, we can understand the process that emplaced the hot TNOs and shut off collisional grinding, leaving the Kuiper Belt with the size distribution we observe today.

The authors acknowledge the sacred nature of Maunakea and appreciate the opportunity to observe from the mountain. CFHT is operated by the National Research Council (NRC) of Canada, the Institute National des Sciences de l'Universe of the Centre National de la Recherche Scientifique (CNRS) of France, and the University of Hawaii, with OSSOS receiving additional access due to contributions from the Institute of Astronomy and Astrophysics, Academia Sinica, Taiwan. Data are produced and hosted at the Canadian Astronomy Data Centre; processing and analysis were performed using computing and storage capacity provided by the Canadian Advanced Network For Astronomy Research (CANFAR).

S.M.L. gratefully acknowledges support from the NRC-Canada Plaskett Fellowship. M.T.B. appreciates support from UK STFC grant ST/L000709/1. W.F. acknowledges support from Science and Technology Facilities Council grant ST/P0003094/1. This project was funded by the National Science and Engineering Research Council and the National Research Council of Canada.

Facility: CFHT (MegaPrime).

Software: matplotlib (Hunter 2007), scipy (Jones et al. 2001).

Appendix

The Appendix comprises Table 3.

Table 3
Centaurs and Scattering TNOs in the OSSOS Survey Ensemble

Dynamical Class[a]	Survey Name	r-band Magnitude[b]	H_r[b]	Distance at Discovery (au)	a (au)	e	i (degrees)	MPC desig.[c]
sca	o3e01	21.50	7.73	23.291	34.416173	0.589571	7.711	K02GG6G
sca	o3e11	23.60	7.86	36.851	86.729341	0.609269	18.362	K13GD6Z
sca	o3l01	23.06	10.89	16.046	55.817595	0.719066	22.246	K13U15R
sca	o3l65	24.14	7.51	45.138	44.608588	0.277799	11.207	K13U16Z
sca	o3o14	23.54	8.00	35.456	143.317456	0.754854	8.580	K13J64O
sca	o3o16	23.92	8.34	35.680	57.383825	0.435939	13.701	K13J64P
sca	o3o17	24.31	8.71	35.811	77.572262	0.540647	10.459	K13J64R
sca	o3o36	23.73	6.09	57.342	49.020848	0.544507	34.879	K13J64Q
sca	o4h03	22.69	9.55	20.758	49.901041	0.779420	5.679	K14UM9Q
sca	o4h04	24.59	11.23	21.916	35.028185	0.376088	31.276	K14UM9A
sca	o4h67PD	23.07	9.49	22.886	38.083254	0.654259	4.960	K06QI0P
sca	o5c002	23.74	11.18	17.958	33.555021	0.524814	15.414	⋯
sca	o5c022	23.68	8.30	34.284	71.897316	0.528607	5.612	⋯
sca	o5c101	23.79	6.58	52.291	98.388020	0.646235	4.287	⋯
sca	o5d002	24.95	10.36	28.844	41.040976	0.301831	34.818	⋯
sca	o5d020	24.54	9.14	34.655	44.202910	0.278006	7.719	⋯
sca	o5d025	24.19	8.60	36.217	68.621838	0.487903	2.105	⋯
sca	o5d034	23.91	8.08	38.181	115.493325	0.777844	22.481	⋯
sca	o5m03	23.94	12.85	12.879	89.174138	0.873805	38.666	⋯
sca	o5m04	24.38	10.19	26.018	32.488890	0.225414	7.026	⋯
sca	o5m52	24.27	8.12	41.057	680.202784	0.940468	13.994	K15KG3G
sca	o5p009	24.07	9.20	30.845	184.132849	0.919622	53.315	⋯
sca	o5p019	22.94	7.55	34.605	31.378013	0.302694	28.288	⋯
sca	o5p021	24.71	9.27	35.180	45.967151	0.249269	11.745	⋯
sca	o5p024	22.80	7.30	35.900	94.674918	0.629258	24.631	⋯
sca	o5p025	22.66	7.08	36.250	100.871870	0.642654	4.771	⋯
sca	o5p060	24.46	8.34	40.983	311.768577	0.876807	8.795	K15G50T
sca	o5p146	24.09	6.47	57.872	85.613291	0.604676	14.247	⋯
sca	o5s06	22.90	8.53	26.576	56.481339	0.531203	13.304	K15RO5W
sca	o5s10	24.22	8.89	33.472	101.338298	0.687477	18.054	⋯
sca	o5s11	24.54	9.14	33.969	50.814125	0.394573	15.159	⋯
sca	o5s13	24.55	9.09	34.254	226.592608	0.861874	6.031	K15RO5Y
sca	o5s20	24.04	8.24	37.139	42.894088	0.241075	6.932	⋯
sca	o5t04	22.99	9.32	22.722	30.988803	0.289815	13.747	K15RO5U
sca	o5t05	24.16	8.80	33.518	126.448249	0.735055	19.83	⋯
sca	o5t06	24.20	8.79	33.933	72.064128	0.534457	12.327	⋯
sca	o5t50	24.32	7.12	51.422	59.872018	0.688095	30.267	⋯
sca	o5t52	24.13	6.10	62.394	425.861136	0.893065	12.138	K15RO5X
sca	L3h08	23.59	7.66	38.445	159.681973	0.761413	15.500	K03H57B
sca	L3q01	23.30	7.46	38.171	51.054204	0.484715	6.922	K03QB3W
sca	L4k09	22.94	8.63	26.634	30.191945	0.185168	13.586	K04K18V
sca	L4m01	23.05	8.05	31.360	33.467236	0.332719	8.205	K04M08W
sca	L4p07	21.71	6.96	29.586	39.953648	0.280856	23.545	K04PB7Y
sca	L4v04	23.44	8.39	31.848	64.100391	0.506381	13.642	K04VD1G
sca	L4v11	23.49	9.24	26.757	60.035908	0.629283	11.972	K04VD1H
sca	L4v15	21.77	8.21	22.950	68.385618	0.698262	14.032	K04VD1M
sca	L7a03	23.14	6.41	46.991	59.613266	0.439491	4.575	K06BS4S
sca	HL7j2	23.37	7.50	37.377	133.932936	0.725235	34.197	K07L38H
sca	HL8a1	22.93	6.29	44.517	32.392864	0.374396	42.826	K08AD8U
sca	HL8n1	23.73	8.52	31.849	41.531221	0.491379	103.447	K08K42V
sca	HL9m1	21.13	9.57	12.872	348.905416	0.968470	68.016	K09M09S
cen	o3l02	23.91	11.47	17.045	19.327805	0.127022	32.476	K13U17C
cen	o3l03	24.39	10.25	25.336	25.872108	0.249698	8.515	K13U17U
cen	o3o01	23.39	11.95	13.774	22.144387	0.378570	32.021	K13J64C
cen	o4h01	22.74	10.29	17.756	23.195009	0.377843	21.319	K14UM5J
cen	o4h02	24.33	11.47	19.526	27.954961	0.440821	12.242	K14UM9G
cen	o5c001	23.72	11.75	15.857	28.529138	0.457119	36.539	⋯
cen	o5d001	23.93	12.74	13.286	28.271438	0.542533	5.729	⋯
cen	o5p001	24.05	13.40	12.029	12.048082	0.082638	24.112	⋯
cen	o5p003	21.39	10.15	13.563	18.145145	0.269879	3.070	⋯
cen	o5p004	23.92	12.68	13.563	20.995607	0.420656	1.628	⋯
cen	o5p005	24.34	10.67	23.501	22.225868	0.257298	11.401	⋯
cen	o5s04	24.51	13.11	13.441	20.915615	0.508346	10.109	⋯

Table 3
(Continued)

Dynamical Class[a]	Survey Name	r-band Magnitude[b]	H_r[b]	Distance at Discovery (au)	a (au)	e	i (degrees)	MPC desig.[c]
cen	o5s05	23.21	10.10	19.884	21.981271	0.479320	15.389	K15RO5V
cen	o5t02	24.91	14.51	10.616	21.692667	0.519340	0.927	⋯
cen	o5t03	23.27	10.48	18.515	25.967473	0.288012	18.849	⋯
cen	mah01	24.45	10.86	22.432	30.072429	0.259122	53.886	K12UH7W
cen	mal01	22.58	9.57	20.296	19.091885	0.176854	10.811	K11Q99F

Notes. All decimal places listed are significant. The full data set is available in Bannister et al. (2018).
[a] Scattering TNOs are designated by "sca," Centaurs by "cen." These and all dynamical classifications within OSSOS use the classification scheme from Gladman et al. (2008).
[b] As noted in Section 3, all measurements have been transposed to r-band assuming $g - r = 0.7$.
[c] https://www.minorplanetcenter.net/iau/info/PackedDes.html

ORCID iDs

S. M. Lawler https://orcid.org/0000-0001-5368-386X
C. Shankman https://orcid.org/0000-0002-3507-5964
J. J. Kavelaars https://orcid.org/0000-0001-7032-5255
M. Alexandersen https://orcid.org/0000-0003-4143-8589
M. T. Bannister https://orcid.org/0000-0003-3257-4490
Ying-Tung Chen (陳英同) https://orcid.org/0000-0001-7244-6069
W. C. Fraser https://orcid.org/0000-0001-6680-6558
J.-M. Petit https://orcid.org/0000-0003-0407-2266
K. Volk https://orcid.org/0000-0001-8736-236X

References

Alexandersen, M., Gladman, B., Greenstreet, S., et al. 2013, Sci, 341, 994
Alexandersen, M., Gladman, B., Kavelaars, J. J., et al. 2016, AJ, 152, 111
Anderson, T. W., & Darling, D. A. 1954, Journal of the American Statistical Association, 49, 765
Bannister, M. T., Gladman, B. J., & Kavelaars, J. J. 2018, ApJS, in press
Bannister, M. T., Kavelaars, J. J., Petit, J.-M., et al. 2016, AJ, 152, 70
Bannister, M. T., Shankman, C., Volk, K., et al. 2017, AJ, 153, 262
Bauer, J. M., Grav, T., Fernández, Y. R., et al. 2017, AJ, 154, 53
Bernstein, G. M., Trilling, D. E., Allen, R. L., et al. 2004, AJ, 128, 1364
Bottke, W. F., Durda, D. D., Nesvorný, D., et al. 2005, Icar, 175, 111
Brasser, R., Schwamb, M. E., Lykawka, P. S., & Gomes, R. S. 2012, MNRAS, 420, 3396
Dohnanyi, J. S. 1969, JGR, 74, 2531
Duffard, R., Pinilla-Alonso, N., Santos-Sanz, P., et al. 2014, A&A, 564, A92
Fernández, Y. R., Kelley, M. S., Lamy, P. L., et al. 2013, Icar, 226, 1138
Fraser, W. C., Brown, M. E., Morbidelli, A., Parker, A., & Batygin, K. 2014, ApJ, 782, 100
Fraser, W. C., & Kavelaars, J. J. 2009, AJ, 137, 72
Fraser, W. C., Kavelaars, J. J., Holman, M. J., et al. 2008, Icar, 195, 827
Fuentes, C. I., & Holman, M. J. 2008, AJ, 136, 83
Gladman, B. 2005, Sci, 307, 71
Gladman, B., & Chan, C. 2006, ApJL, 643, L135
Gladman, B., Kavelaars, J. J., Petit, J.-M., et al. 2001, AJ, 122, 1051
Gladman, B., Lawler, S. M., Petit, J.-M., et al. 2012, AJ, 144, 23
Gladman, B., Marsden, B. G., & Vanlaerhoven, C. 2008, in The Solar System Beyond Neptune, ed. M. A. Barucci et al. (Tucson, AZ: Univ. Arizona Press), 43
Gomes, R. S., Fernández, J. A., Gallardo, T., & Brunini, A. 2008, in The Solar System Beyond Neptune, ed. M. A. Barucci et al. (Tuscon, AZ: Univ. Arizona Press), 259
Gomes, R. S., Morbidelli, A., & Levison, H. F. 2004, Icar, 170, 492
Gomes, R. S., Soares, J. S., & Brasser, R. 2015, Icar, 258, 37
Greenstreet, S., Gladman, B., & McKinnon, W. B. 2015, Icar, 258, 267
Hahn, J. M., & Malhotra, R. 2005, AJ, 130, 2392
Holman, M. J., Payne, M. J., Fraser, W., et al. 2018, ApJL, 855, L6
Hunter, J. D. 2007, CSE, 9, 90
Irwin, M., Tremaine, S., & Zytkow, A. N. 1995, AJ, 110, 3082
Jewitt, D., Luu, J., & Chen, J. 1996, AJ, 112, 1225
Jewitt, D., Weaver, H., Agarwal, J., Mutchler, M., & Drahus, M. 2010, Natur, 467, 817
Jones, E., Oliphant, T., Peterson, P., et al. 2001, SciPy: Open source scientific tools for Python, https://www.scipy.org/
Kaib, N. A., Becker, A. C., Jones, R. L., et al. 2009, ApJ, 695, 268
Kaib, N. A., Roškar, R., & Quinn, T. 2011, Icar, 215, 491
Kavelaars, J. J., Jones, R. L., Gladman, B. J., et al. 2009, AJ, 137, 4917
Lawler, S. M., Kavelaars, J., Alexandersen, M., et al. 2018, arXiv:1802.00460
Malhotra, R. 1995, AJ, 110, 420
Moore, J. M., McKinnon, W. B., Spencer, J. R., et al. 2016, Sci, 351, 1284
Morbidelli, A., Bottke, W. F., Nesvorný, D., & Levison, H. F. 2009a, Icar, 204, 558
Morbidelli, A., Levison, H. F., Bottke, W. F., Dones, L., & Nesvorný, D. 2009b, Icar, 202, 310
Morbidelli, A., Levison, H. F., Tsiganis, K., & Gomes, R. 2005, Natur, 435, 462
Nesvorný, D. 2015, AJ, 150, 73
Nesvorný, D., & Vokrouhlický, D. 2016, ApJ, 825, 94
Nesvorný, D., Vokrouhlický, D., & Morbidelli, A. 2013, ApJ, 768, 45
Pan, M., & Schlichting, H. E. 2012, ApJ, 747, 113
Parker, A. H. 2015, Icar, 247, 112
Peixinho, N., Delsanti, A., & Doressoundiram, A. 2015, A&A, 577, A35
Petit, J., Kavelaars, J. J., Gladman, B., et al. 2011, AJ, 142, 131
Petit, J.-M., Kavelaars, J. J., Gladman, B., & Loredo, T. 2008, in The Solar System Beyond Neptune, ed. M. A. Barucci et al. (Tucson, AZ: Univ. Arizona Press), 71
Petit, J.-M., Kavelaars, J. J., Gladman, B. J., et al. 2017, AJ, 153, 236
Schlichting, H. E., Fuentes, C. I., & Trilling, D. E. 2013, AJ, 146, 36
Shankman, C., Gladman, B. J., Kaib, N., Kavelaars, J. J., & Petit, J. M. 2013, ApJL, 764, L2
Shankman, C., Kavelaars, J., Gladman, B. J., et al. 2016, AJ, 151, 31
Shannon, A., Wu, Y., & Lithwick, Y. 2016, ApJ, 818, 175
Sheppard, S. S., & Trujillo, C. A. 2010, ApJL, 723, L233
Singer, K. N., McKinnon, W. B., & Gladman, B. 2018, Sci, submitted
Singer, K. N., McKinnon, W. B., Robbins, S. J., et al. 2016, 47th Lunar and Planetary Science Conf. (Houston, TX: LPI), 2310
Snodgrass, C., Fitzsimmons, A., Lowry, S. C., & Weissman, P. 2011, MNRAS, 414, 458
Stern, S. A., Bagenal, F., Ennico, K., et al. 2015, Sci, 350, aad1815
Tegler, S. C., Romanishin, W., & Consolmagno, G. J. 2016, AJ, 152, 210
Tsiganis, K., Gomes, R., Morbidelli, A., & Levison, H. F. 2005, Natur, 435, 459
Volk, K., & Malhotra, R. 2008, ApJ, 687, 714
Volk, K., Murray-Clay, R., Gladman, B., et al. 2016, AJ, 152, 23
Volk, K., Murray-Clay, R., Gladman, B., et al. 2017, in AAS/DPS Meeting 49 Abstracts, 216.12
Wong, I., & Brown, M. E. 2015, AJ, 150, 174
Yoshida, F., & Terai, T. 2017, AJ, 154, 71